Effect of hydrodynamic flow on low-field spin-lattice relaxation in liquids in the nanoscopic vicinity of solid surfaces: Theory and Monte Carlo simulations of model pore spaces

Carlos Mattea, Hernan Tiraboschi, and Rainer Kimmich
Sektion Kernresonanzspektroskopie, Universität Ulm, 89069 Ulm, Germany
(Received 19 April 2005; published 22 August 2005)

It is shown that slow hydrodynamic flow with velocities of a few millimeters per second reduces the spin-lattice relaxation rate of fluids confined to pores of a diamagnetic, polar, solid material. The effect is predicted by an analytical theory and Monte Carlo simulations of model pore spaces. Adsorbate molecules diffusing in the vicinity of pore surfaces can perform adsorption, desorption, and readsorption cycles, effectively leading to displacements along the surface (also termed "bulk mediated surface diffusion" or BMSD). Since the surface determines the orientation of the adsorbed molecule relative to the external magnetic field, desorption at one site and readsorption at another site of a nonplanar surface will cause molecular reorientation. This is the basis of the "reorientation mediated by translational displacements" (RMTD) relaxation mechanism. If hydrodynamic flow is superimposed on diffusion, the RMTD process will be accelerated in a sort of rotational analog to translational hydrodynamic (or Taylor-Aris) dispersion. This reveals itself by a prolongation of spin-lattice relaxation times at low frequencies. The flow-relaxation effect takes place in the vicinity of the pore surfaces on the order of nanometers. The conclusions are (i) the BMSD and RMTD relaxation mechanism of fluids in porous materials is corroborated, (ii) hydrodynamic dispersion affects molecular displacements at surfaces, and (iii) interfacial slip in the sense of a molecular hopping, i.e., a desorption-readsorption process takes place.

DOI: 10.1103/PhysRevE.72.021602 PACS number(s): 47.55.Mh, 76.60.Es, 82.56.Na, 83.50.Lh

I. INTRODUCTION

The objective of this study is to examine the influence of hydrodynamic flow on low-frequency spin-lattice relaxation in fluids confined in microporous media analytically and numerically. The envisaged frequency and time scales are $10^3 < \nu < 10^8$ Hz and $10^{-9} < t < 10^{-4}$ s, respectively, corresponding to field-cycling NMR relaxometry [1]. Following our previous report [2], the motivation to do so has three aspects.

First, this sort of study is suitable to elucidate the low-field spin-lattice relaxation mechanism for strong adsorbate fluids in porous media suggested in Refs. [3,4]. Dipolar and quadrupolar orientation correlation times up to seven orders of magnitude longer than in the bulk fluid were observed in nanoporous materials. The explanation was the so-called reorientation mediated by translational displacements (RMTD) process. Adsorbate molecules are subject to frequent adsorption-desorption-readsorption cycles at the pore walls [5]. Bulk mediated surface diffusion (BMSD) produces Lévy-walk-like displacements along the pore surface [5–8], which explain how the adsorbate molecules probe the surface topology with respect to the orientation relative to the main magnetic field [4,9,10]. Under such conditions hydrodynamic flow superimposed on surface diffusion is expected to accelerate the RMTD process (see Fig. 1).

Second, hydrodynamic (or Taylor-Aris) dispersion [11,12], that is, the superposition of incoherent Brownian particle motions and coherent flow, is of general interest [13–18]. In the vicinity of surfaces the question arises whether interfacial slip exists. Since we are dealing with a surface relaxation process, a detailed examination of the valid flow boundary condition is possible.

Finally, field-cycling NMR relaxometry [1] probes molecular mechanisms on a time scale up to 10^{-4} s. That is, molecular root mean square displacements by Brownian motions are much less than 100 nm in water at room temperature. Flow can therefore influence surface relaxation only in a surface layer thinner than 100 nm. In a sense, nanofluidics can be examined on this basis.

The flow and relaxation scenario considered here is illustrated in Fig. 1. The model refers to a liquid in the pore space of a porous medium. We distinguish the phase of molecules adsorbed at the surface from the bulklike phase. On the time scale of the proton spin-lattice relaxation times, which is for field-cycling relaxometry typically $10\ \text{ms} < T_1 < 1$ s, fast molecular exchange between the two phases occurs. Hydrodynamic flow is assumed to be superimposed on Brownian motion of the molecules. In case the liquid molecules and the pore surfaces are both polar, molecules in the vicinity of the surfaces will be subject to adsorption and desorption kinetics including possible readsorption cycles. The reorientation of molecules that happen to be adsorbed initially as well as finally will thus depend on displacements and readsorption at a more or less distant surface site of a different orientation. These displacements are the combined result of Brownian motions and laminar flow, that is, hydrodynamic dispersion.

The hydrodynamic dispersion properties are usually characterized by the Péclet number defined by

$$\text{Pe} = \frac{f\xi}{wD_m}, \tag{1}$$

where ξ is the correlation length of the pore space, f is the hydrodynamic flux, D_m is the molecular diffusion constant in the bulk, and w is the pore width. In the following the Péclet number will be taken as a measure of the mean flow velocity relative to Brownian diffusion.

Following the bulk mediated surface diffusion formalism of Bychuk and O'Shaughnessy [5,6] different adsorption and desorption probabilities per time unit, Q_{ads} and Q_{des}, respectively, can be distinguished. The adsorption on surfaces can be characterized by a number of characteristic parameters. The retention time t_h reflects how long it takes until the initial adsorbate population on a surface is finally replaced by molecules initially in the bulklike phase. The retention time is related to the so-called adsorption depth h according to

$$t_h = \frac{h^2}{D_m}. \tag{2}$$

On the other hand, the adsorption length can be expressed by

$$h = \lambda \frac{Q_{ads}}{Q_{des}}, \tag{3}$$

where λ is the "capture range" within which a molecule can directly be adsorbed on the surface. This equation is based on a dynamic equilibrium of the one-dimensional "reaction-diffusion" process as which adsorption and translational diffusion to and from the surface can be interpreted. The time scale of desorption-diffusion-readsorption cycles is given by $Q_{des}^{-1} < t < t_h$, and was shown to be of the same order of magnitude as the time scale probed by field-cycling NMR relaxometry [1,4].

The weak-adsorption limit is characterized by

$$t_h Q_{des} \ll 1. \tag{4}$$

That is, the adsorbate molecules are most likely exchanged to the bulklike phase immediately after desorption. This is in contrast to the strong-adsorption limit

$$t_h Q_{des} \gg 1, \tag{5}$$

in which numerous desorption-readsorption cycles occur before an adsorbate molecule finally disappears in the bulklike phase. This strong-adsorption limit must be assumed for a combination of polar adsorbate molecules and polar surfaces [3,4]. In the present study we are dealing with this case.

In Sec. II a general analytical formalism will be outlined for the flow-relaxation effect in terms of the dipolar autocorrelation function and spectral density. Representing the pore space by a number of simplified model structures permits one to examine the principal properties of this effect with the aid of Monte Carlo simulations as described in Sec. III. The results of analytical model treatments specific for those model structures will be compared and fitted to the evaluations of the simulations. Finally we will discuss the intricacies of experimental verifications of the flow-relaxation effect.

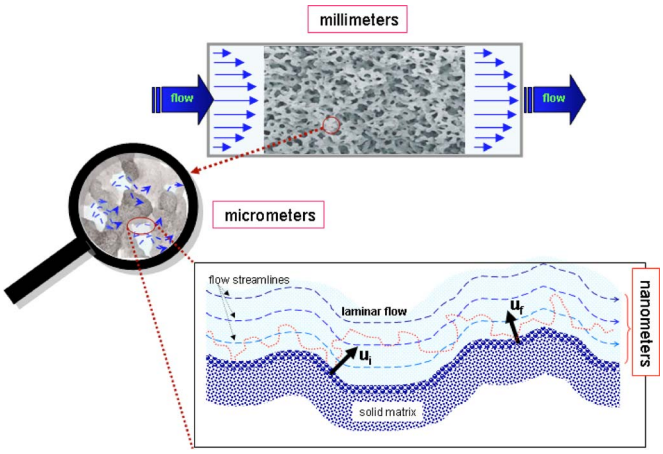

FIG. 1. (Color online) Illustration of the flow-relaxation effect and adsorbate reorientation by hydrodynamic dispersion. A liquid is pressed through a porous sample (top part of the figure). The liquid flows along the pore surfaces (bottom part of the figure). The dotted line represents a trajectory of a molecule by Brownian motion in the presence of laminar flow along the surface. Flow streamlines are drawn as broken lines. The adsorption layer on the solid matrix is indicated. The arrows refer to the local preferential orientations of molecules at the initial and final pore surface sites. The thickness of the fluid layer along the surface in which the flow enhanced RMTD process is expected to take place ranges from molecular diameters up to about 100 nm.

II. GENERAL THEORY OF THE FLOW-NMR-RELAXATION EFFECT

The spin-lattice relaxation rate of a two-spin-1/2 system ensemble of like nuclei subject to dipolar coupling is given by [19,20]

$$\frac{1}{T_1} = K[I(\omega) + 4I(2\omega)], \tag{6}$$

where K is a constant determined by the type and strength of the spin interaction. The spectral density (or intensity function) $I(\omega)$ depends on the resonance angular frequency $\omega = \gamma B_0$, where γ is the gyromagnetic ratio and B_0 is the flux density of the main magnetic field. The spectral density is the

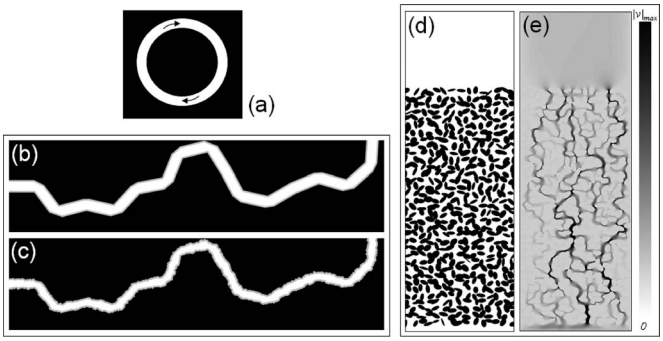

FIG. 2. The diverse geometries of two-dimensional pore spaces used for the Monte Carlo simulations. The pores are represented in white. (a) Circular pore. Random-walk-shaped pipes with (b) smooth and (c) rough surfaces. (d) Ellipsoidal-grain pack. (e) Map of the magnitudes of the flow velocity simulated with the finite volume method for the ellipsoidal-grain pack. The velocity field obtained in this way was used for the Monte Carlo simulations of the flow-relaxation effect described in Sec. IV B 3.

Fourier transform of the autocorrelation function $G(t)$. For intramolecular dipolar interaction (which is relevant here [3,4]), $G(t)$ refers to spherical harmonics of second order characterizing the orientation of the two-spin system relative to the main magnetic field. That is, spin-lattice relaxation probes molecular reorientations.

Spin-lattice relaxation in porous media at frequencies much less than the bulk reorentation rates of the molecules was shown to be governed by the RMTD mechanism at the pore surfaces [4,9,20]. The problem is now to generalize this formalism for superimposed hydrodynamic flow, i.e., hydrodynamic dispersion.

The curvilinear coordinate along a streamline along the surface will be defined as x (see Fig. 1). Descriptions of hydrodynamic dispersion in bulk fluids can be found in Refs. [21–24]. For scalar fields and incompressible fluids, the convective-diffusion equation applies:

$$\frac{\partial \Psi}{\partial t} + \vec{V} \cdot \nabla \Psi = \tilde{D} \cdot \nabla^2 \Psi. \tag{7}$$

The function Ψ is the propagator, $\vec{V}$ is the average over the local velocities $\vec{v}$, and $\tilde{D}$ is the dispersion tensor. In the case of macroscopically homogeneous and isotropic porous media, $\tilde{D}$ can be decomposed into the components $D_\perp$ and $D_\parallel$ orthogonal and parallel to the flow velocity $\vec{V}$, respectively. The convective-diffusion equation then becomes

$$\frac{\partial \Psi}{\partial t} + \vec{V} \cdot \nabla \Psi = D_\perp \nabla_\perp^2 \Psi + D_\parallel \frac{\partial^2 \Psi}{\partial \mathbf{x}^2}, \tag{8}$$

where $\nabla_\perp^2$ is the Laplace operator in the transverse direction. The dispersion coefficients $D_\perp$ and $D_\parallel$ depend on the flow velocity, of course. In the limit of vanishing flow velocities, $D_\parallel$ becomes equal to the molecular diffusion coefficient (D_m) diminished by the tortuosity factor.

In the present context, only the longitudinal version of hydrodynamic dispersion is of interest, that is, the projection of Eq. (8) on the x direction. In this case, $D=D_\parallel$ can be equated. After Fourier transformation the solution is

$$\psi(k,t) = \hat{\psi}(k) e^{-Dtk^2} e^{-ikvt}, \tag{9}$$

where $\hat{\psi}(k)$ is the Fourier transform of $\Psi(x,0)$ and v is the velocity component in longitudinal direction. The "wave number" k is the reciprocal-space variable conjugate to the real-space variable x. With the initial condition $\Psi(x,0) = c_0 \delta(x)$ the conjugate Fourier expression reads

$$\Psi(x,t) = \frac{c_0}{2\pi} \int_{-\infty}^{+\infty} e^{-(Dtk^2+ikvt)} e^{ixk} dk. \tag{10}$$

Note that the Gaussian term in the propagator given in Eq. (9) or Eq. (10) anticipates ordinary diffusion. There is some argument based on the BMSD model by Bychuk and O'Shaughnessy [5,6,8] that features of Lévy walks along the surface are relevant so that a Cauchy propagator would be more appropriate [3,4,25]. For simplicity we will restrict ourselves in the analytical treatment to the ordinary diffusion case. The objective of the present study is to reveal the influence of coherent flow on spin-lattice relaxation whereas the type of diffusion process is considered to be of minor importance in this context. The Monte Carlo simulations should anyway reflect the actual propagators, of course.

The autocorrelation function describing orientational fluctuations of molecules with fixed intramolecular interdipole distances can be expressed by [19,20]

$$G(t) = 4\pi \langle Y_{2,m}(\vec{u}_i) Y_{2,-m}(\vec{u}_f) \rangle_{\vec{u}_i,\vec{u}_f} = \int \langle P_c(\vec{u}_i,\vec{u}_f,t) Y_{2,m}(\vec{u}_i) \rangle_{\vec{u}_i} Y_{2,-m}(\vec{u}_f) d\Omega_f, \tag{11}$$

where the angular brackets indicate ensemble averages. $\vec{u}_i$ and $\vec{u}_f$ are unit vectors normal to the surface indicating the initial and the final orientations of the molecule under consideration (see Fig. 1). $d\Omega_f$ is the differential solid angle into which $\vec{u}_f$ points. In the usual spin-lattice relaxation theory of dipolar coupled like spins subscripts $m=1$ and 2 occur [19,20]. However, no distinction will be made in the following since this causes only minor differences in the results. In the Monte Carlo simulations even the value $m=0$ will be used for simplicity without loss of validity of the principle [26].

The conditional probability density can be expressed as

$$P_c(\vec{u}_i,\vec{u}_f,t) = \int_{-\infty}^{\infty} \Theta(\vec{u}_i,\vec{u}_f,x) \Psi(x,t) dx, \tag{12}$$

where $\Psi(x,t)$ is the surface diffusion propagator, i.e., the probability density that the adsorbate molecule is displaced by a curvilinear distance x along the surface in an interval t, and $\Theta(\vec{u}_i,\vec{u}_f,x)$ is the probability that the surface orientation changes from $\vec{u}_i$ to $\vec{u}_f$ in a curvilinear distance x.

Using the expansion in terms of spherical harmonics with the initial condition $\Theta(\vec{u}_i,\vec{u}_f,0) = \delta(\vec{u}_f - \vec{u}_i)$ the surface orientation probability density becomes

$$\Theta(\vec{u}_i,\vec{u}_f,x) = \sum_{l',m'} Y_{l',-m'}(\vec{u}_i) Y_{l',m'}(\vec{u}_f) g(x), \tag{13}$$

where $g(x)$ is the normalized surface orientation correlation function between surface sites separated by a curvilinear distance x. "Normalized" means that $g(x=0)=1$. The combination of Eqs. (11)–(13), and making use of the orthonormal properties of spherical harmonics, leads to

$$G(t) = \int_{-\infty}^{\infty} g(x) \Psi(x,t) dx. \tag{14}$$

Inserting the propagator given in Eq. (10) in Eq. (14) leads to

$$G(t) = \int_{-\infty}^{+\infty} g(x) \left(\frac{c_0}{2\pi} \int_{-\infty}^{+\infty} e^{-(Dtk^2+ikvt)} e^{ikx} dk \right) dx. \tag{15}$$

Regrouping the factors that depend only on the space variable x results in the orientational structure factor

$$S(k) = \frac{c_0}{2\pi}\int_{-\infty}^{+\infty} g(x)e^{ikx}dx. \tag{16}$$

The autocorrelation function given in Eq. (11) can thus be rewritten as

$$G(t) = \int_{-\infty}^{+\infty} S(k)e^{-(Dtk^2+ikvt)}dk. \tag{17}$$

A typical application of this general formula to the case of a simple circular pore is given in Eq. (27). Treatments of other pore-space structures will follow.

The Fourier transform of Eq. (17) is the corresponding spectral density. Its real part reads

$$I(\omega) = \int_{-\infty}^{+\infty} S(k)\frac{2Dk^2}{(Dk^2)^2 + (kv+\omega)^2}dk. \tag{18}$$

Up to now a given flow velocity v was assumed. In reality one expects a distribution of flow velocities, $P(v)$. Averaging the above expression on this basis leads to

$$I(\omega) = \int_{v_{min}}^{v_{max}} P(v)\int_{-\infty}^{+\infty} S(k)\frac{2Dk^2}{(Dk^2)^2 + (kv+\omega)^2}dk\,dv, \tag{19}$$

where v_{min} and v_{max} indicate the velocity range. Combining this expression for the spectral density with Eq. (6) provides a velocity dependent spin-lattice rate. The influence of flow velocity on spin-lattice relaxation will be called the flow-relaxation effect.

III. DETAILED THEORY FOR THE MONTE CARLO SIMULATIONS

A. Definitions

The flow-relaxation effect predicted by Eq. (19) was further examined with the aid of Monte Carlo simulations for a number of simple model structures (see Fig. 2). For the sake of simplicity we restrict ourselves to two-dimensional representations of pores and grain packs. The sole objective of this model treatment is to reveal the relationship between the pore-space structure and the resulting flow-relaxation effect in systems of tractable complexity.

The simulations selectively refer to molecules contributing to the initial surface population. Molecules being initially adsorbed can be subject to three different dynamic evolutions during the time interval to which the autocorrelation function refers. (i) They remain (and possibly diffuse translationally) within the adsorption layer so that they are finally still adsorbed. (ii) They get exchanged with molecules that were initially in the bulklike phase but get readsorbed somewhere on the surface so that they are finally in the adsorbed phase again. (iii) They get exchanged with molecules that were initially in the bulklike phase and reside there finally.

Since the bulklike phase is characterized by rapid rotational diffusion, only the first two cases can retain orientational correlation. We attribute the correlation function $G_{reo}(t)$ to molecules being subject to these two types of dynamic evolution.

On the other hand, initially adsorbed molecules being subject to case (iii) cannot retain any correlated orientations. One may speak of "exchange losses" and attribute a correlation function $G_{ex}(t)$ to this sort of correlation decay.

These two classes of correlation functions are stochastically independent from each other since both can be considered as the result of a large number of random elementary processes and diffusion steps. The total correlation function expected to be relevant for experiments can then be written as a product in the form

$$G_T(t) = G_{ex}(t)G_{reo}(t). \tag{20}$$

The displacement of particles is mimicked by Monte Carlo generated random walks of fixed step length σ and a superimposed velocity field representing laminar flow. The starting position is chosen at random on the surface. In the

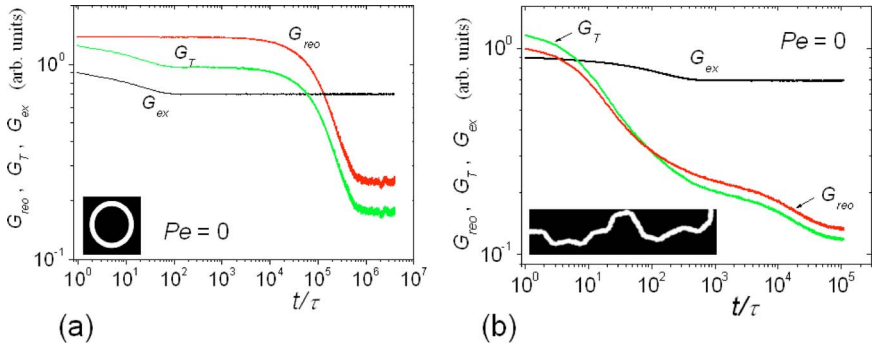

FIG. 3. (Color online) Typical reorientation autocorrelation functions in the absence of flow. (a) Simulation for the two-dimensional circular pore with smooth surfaces schematically shown in the inset. The reorientation and exchange time scales are different enough to identify two corresponding steps in the decay of the total correlation function G_T. The step at short times is obviously due to (velocity independent) exchange losses as demonstrated by the function G_{ex}. The second step at long times must be attributed to the (velocity dependent) reorientational part $G_{reo}=G_T/G_{ex}$. (b) Simulation for the two-dimensional random-walk-shaped pore with rough surfaces schematically shown in the inset. In this case, the two time scales overlap, so that the two sorts of losses do not appear as separate steps in the decay of the total correlation function. The two plots visualize the different behavior for smooth and rough surface topologies. Qualitatively the same tendencies are observed for any of the pore-space geometries shown in Fig. 2.

channel-like pore structures [Figs. 2(a)–2(c)], a parabolic velocity profile about the channel axis was assumed. The velocity field taken for the ellipsoidal-grain pack model [Fig. 2(d)] was simulated with the aid of a computational fluid dynamics technique (software package FLUENT 5.5 based on the finite volume method). The result is represented in Fig. 2(e).

The flux f is given by the integral of the flow velocity over a cross section of the channel. Note that the flux unit in two dimensions is [length]^2/[time] compared to [length]^3/[time] in the three-dimensional case. Instead of assuming cyclic boundary conditions for the noncyclic pore structures shown in Figs. 2(b)–2(d), the simulation runs are stopped and reinitiated whenever the random walker reaches an open end of the structure.

Once a molecule enters an interfacial surface layer of width λ, the so-called capture range, it can get adsorbed. Inside of the interfacial layer the particle is assumed to get adsorbed with the probability Q_{ads} per simulation step (which is taken as time unit). When adsorbed the particle is assumed to get desorbed again with the probability Q_{des} per simulation step.

In the context of the two-dimensional structures shown in Fig. 2, "surface" refers to the lines defining the pore boundaries. Molecular "orientation vector" hence means a vector in the drawing plane defined by the polar angle θ relative to the main magnetic field $\vec{B}_0$, which again is assumed to be an in-plane vector.

B. Evaluation of the correlation function

The Monte Carlo simulations provide the total correlation function which is evaluated according to

$$G_T(t) = \langle C(t) \rangle \tag{21}$$

with

$$C(t) = \begin{cases} Y_{2,m}(\theta_0, \varphi_0) Y_{2,-m}(\theta_s, \varphi_s) & \text{if initially and finally adsorbed,} \\ 0 & \text{otherwise.} \end{cases} \tag{22}$$

The angular brackets indicate an ensemble average. "Otherwise" means that the adsorbate molecule is residing either initially or finally or initially as well as finally in the bulklike phase where rotational diffusion leads to a practically immediate loss of correlation (see Sec. 7.1 in Ref. [1]). That is, the low-frequency relaxation under consideration here is solely due to molecules that are initially and finally in the adsorbed state. The angles θ_0, φ_0 and θ_s, φ_s are the polar coordinates of the surface orientations relative to the main magnetic field at positions $s=0$ at time $t=0$ and s after a time t, respectively. The distance s is measured as a curvilinear length on the surface topology.

All simulations were carried out for $m=0$, i.e., for the spherical harmonics $Y_{2,0}$. The azimuthal angle φ consequently does not matter. In Ref. [26], it was shown that the choice of the subscript m does not influence the results qualitatively. The shortest step time of the molecules is defined by the simulation cycle time τ. For the adsorption and desorption, rates were assumed to be $Q_{ads}=0.99\tau^{-1}$ and $Q_{des}=0.1\tau^{-1}$, respectively (compare the simulations in Ref. [6]).

The exchange loss part of the correlation decay can be simulated by

$$G_{ex}(t) = \langle C_{ex}(t) \rangle \tag{23}$$

and

$$C_{ex}(t) = \begin{cases} 1 & \text{if initially and finally adsorbed,} \\ 0 & \text{otherwise.} \end{cases} \tag{24}$$

The angular brackets indicate an ensemble average again. Starting from $G_{ex}(0)=1$, this function decays with a characteristic time constant τ_{ex}. In the long-time limit, the equilibrium population in the adsorbed phase is approached. Note that this contribution to the total correlation function is independent of the flow velocity.

Dividing G_T by the exchange loss function separately simulated according to Eq. (23) results in the proper RMTD part of the correlation decay,

$$G_{reo} = \frac{G_T}{G_{ex}}. \tag{25}$$

This is the velocity dependent part of the correlation loss and consequently reflects hydrodynamic dispersion. Figure 3 shows typical examples of the contributions to the total correlation function as defined above.

IV. APPLICATION TO MODEL PORE SPACES

The "pore spaces" under consideration were a circular pore [Fig. 2(a)], a chain of randomly oriented, jointed straight pipe sections with smooth [Fig. 2(b)] or rough [Fig. 2(c)] surfaces, and a pack of ellipsoidal grains [Fig. 2(d)]. A fluid is assumed to percolate through such structures. The illustration in Fig. 2(e) shows a typical map of the flow velocity magnitude obtained as a numerical solution of the Navier-Stokes equations applied to the structure shown in Fig. 2(d).

A. Orientational structure factor and simulations for a circular channel

For a two-dimensional circular pore [see Fig. 2(a)] of channel width w which is negligible relative to the mean

circle radius $\bar{R}=(R_{max}+R_{min})/2$, i.e., $w \ll \bar{R}$, an exact solution exists according to the formalism presented above. This type of geometry is characterized by a single wave number $k=k_0=1/\bar{R}$ in a certain analogy to other periodic structures such as the corrugated surface of lipid bilayers in the ripple phase [9,27]. The orientational structure factor is then a δ function,

$$S(k) = c_0 \delta(k - k_0), \tag{26}$$

where c_0 is a constant. Inserting this in Eq. (17) leads to

$$G(t) = c_0 e^{-D_{disp} k_0^2 t} e^{-iv k_0 t} + c_1 = c_0 e^{-\alpha n} e^{-i\beta n} + c_1, \tag{27}$$

where $n=t/\tau$ and D_{disp} is the dispersion coefficient in analogy to the molecular self-diffusion coefficient D_m. Note that $D_{disp}=D_m$ in the static case and $D_{disp}>D_m$, otherwise. The real time is represented by t expressed in units of the simulation cycle time τ. The parameters α and β are given by

$$\alpha = D_{disp} k_0^2 \tau \tag{28}$$

and

$$\beta = k_0 v \tau, \tag{29}$$

respectively. $c_1=\langle Y_{2,m}^2 \rangle$ is a constant accounting for any finite residual correlation in the long-time limit [see Eq. (22)]. The spectral density is given as the Fourier transform of Eq. (27):

$$I(\omega) = \frac{c_0}{2\pi} \frac{\tau\alpha}{\alpha^2 + (\beta + \omega\tau)^2}. \tag{30}$$

This function in turn is the basis for the spin-lattice relaxation rate given in Eq. (6).

For the simulations the outer and inner radii of the circular channel were set as $R_{max}=105\ell$ and $R_{min}=100\ell$, respectively, so that the condition $w \ll \bar{R}$ assumed for the analytical theory is satisfied. ℓ is the length unit on which the Monte Carlo simulations are based. The step length of the random walk was assumed to have the fixed value $\sigma=0.5\ell$.

The correlation length of a circular pore can be estimated in the following way. The orientation correlation function in a circle of radius $\bar{R}$ is

$$\langle \vec{u}(0) \cdot \vec{u}(s) \rangle = \cos(s/\bar{R}), \tag{31}$$

where $\vec{u}(0)$ and $\vec{u}(s)$ are the tangent unit vectors at curvilinear coordinates 0 and s, respectively. The correlation length is then taken as the curvilinear distance on which this correlation function decays to the value $1/e$:

$$\xi = \bar{R} \arccos(1/e) \simeq \bar{R} \times 1.194. \tag{32}$$

For $\bar{R}=(R_{max}+R_{min})/2$ with the above values for R_{max} and R_{min}, the correlation length of the circular pore channel under consideration is $\xi=122.4\ell$. The Péclet number Pe was calculated on this basis according to Eq. (1) as a measure of the relative hydrodynamic flow rate.

Figure 3(a) shows results for the correlation functions G_T, G_{ex}, G_{reo} in the absence of flow. When hydrodynamic flow is turned on, the reorientation correlation function starts to oscillate as a consequence of the periodicity of the cyclic pore

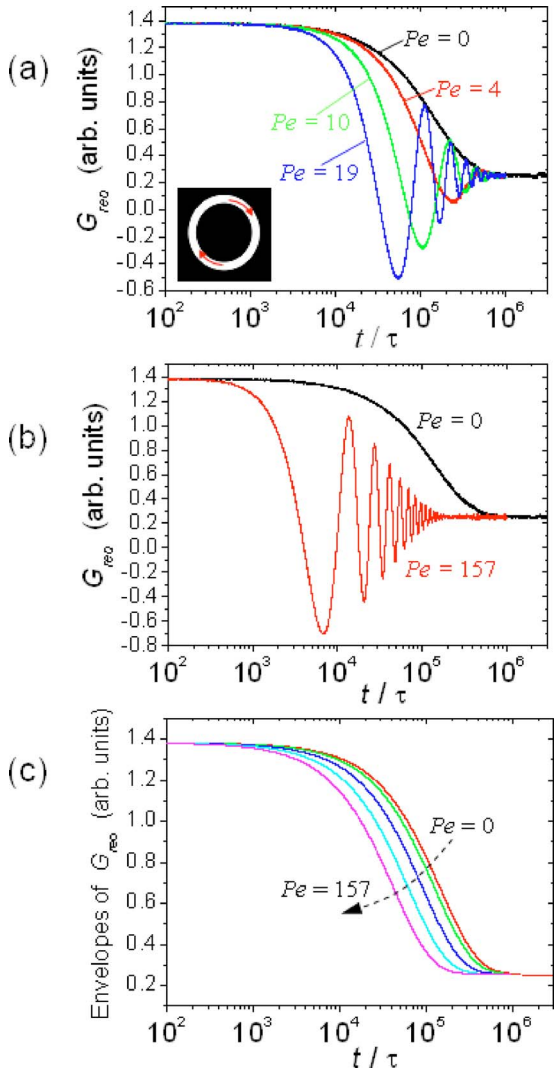

FIG. 4. (Color online) Orientation correlation function G_{reo} for the two-dimensional circular pore model (see inset) resulting from a Monte Carlo simulation. Different flow velocities, that is, different Péclet numbers Pe, were assumed. The oscillations in the presence of flow reflect the periodicity of the structure. Attenuation by hydrodynamic dispersion becomes perceptible only at flow velocities (i.e., Péclet numbers) large enough as expected from the analytical theory [Eq. (27)]. (a) Low flow velocities. The attenuation by hydrodynamic dispersion is negligible. (b) High flow velocity compared to the correlation function in the absence of flow. Attenuation by hydrodynamic dispersion is obvious. (c) Envelopes of the oscillatory functions displayed in (a) and (b). The attenuation with increasing Péclet numbers, i.e., increasing flow velocities, due to hydrodynamic dispersion is obvious. From the top to the bottom the Péclet numbers are 0,39,78,117,157.

(Fig. 4). The oscillatory behavior corresponds to the factor $\exp\{-i\beta n\}$ in Eq. (27). Attenuation by hydrodynamic dispersion [see the factor $\exp\{-\alpha n\}$] becomes more and more effective with increasing flow velocity.

The analytical theory that is the real part of Eq. (27) can be fitted to the results of the Monte Carlo simulations as a function of the hydrodynamic flux. The parameters are listed in Table I. Figure 5 shows the parameter α as a function of

TABLE I. Values of the parameters in Eq. (27) fitted to Monte Carlo simulations of the orientation correlation function for a circular pore (see Fig. 4).

Péclet number	α	β
0.00	6.623×10^{-6}	0.000
1.96	6.623×10^{-6}	5.605×10^{-6}
3.92	6.650×10^{-6}	1.100×10^{-6}
9.79	6.65×10^{-6}	2.740×10^{-5}
19.6	6.90×10^{-6}	5.480×10^{-5}
39.2	7.50×10^{-6}	1.095×10^{-4}
78.3	1.06×10^{-5}	2.190×10^{-4}
117	1.55×10^{-5}	3.28×10^{-4}
157	2.30×10^{-5}	4.36×10^{-4}

the Péclet number (or the mean flow velocity). The fitted data can be represented by a square relationship for the "dispersion parameter" α,

$$\alpha = \alpha_0 + b(\mathrm{Pe})^2, \tag{33}$$

where α_0 and b are constants.

It is worth noting that the local dispersion coefficient in the vicinity of the surface exhibits the universal Aris-Taylor behavior [21]

$$D_{disp} = D_m + \chi\frac{v^2}{D_m}, \tag{34}$$

where χ is a constant related to the geometry of the structure. In a capillary, $\chi=\varrho_s l_s^2/D_m$, where l_s is the length scale of the tube and ϱ_s is a factor that depends on the shape of the cross section [12].

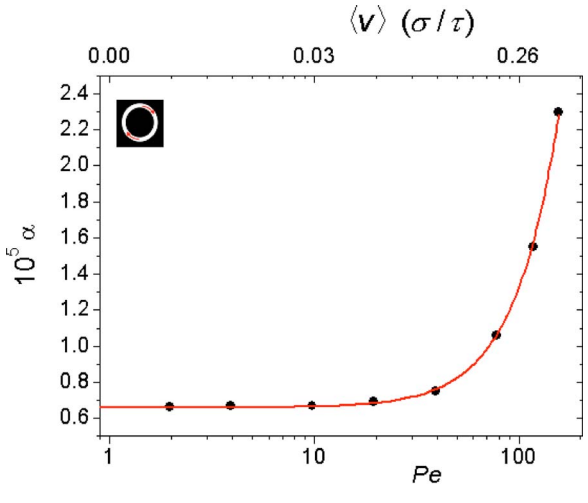

FIG. 5. (Color online) Dispersion parameter α defined in Eq. (27) as a function of the Péclet number (or mean velocity) for a circular channel. The data points were obtained by fitting Eq. (27) to the simulated correlation functions (see Fig. 4). The solid line represents a fit of Eq. (33) to these data points.

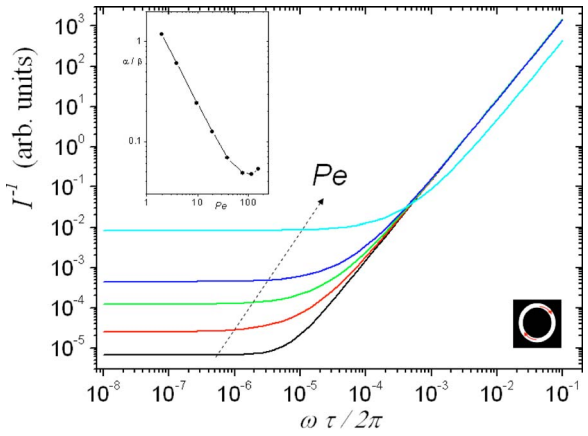

FIG. 6. (Color online) Spectral densities calculated with the aid of Eq. (30) for a circular pore for different fluxes. The pore structure is represented by the symbol in the lower right corner. The parameters α and β were fitted to the simulated correlation functions and are listed in Table I. The Péclet numbers are from the bottom to the top (see arrow) 0,4,10,20,157. The inset plot shows the ratio $\alpha/\beta = k_0 D_{disp}/v$ as a function of the Péclet number. The minimum is related to the shift of the intensity functions for the highest Péclet numbers relative to those for low Péclet numbers (see the curve for Pe ~ 157 in the main plot).

Taking the values of the parameters α and β fitted to the simulated correlation functions [see Eq. (27) and Table I] permits one to calculate the inverse spectral density as a function of the frequency. The relevant formula is given in Eq. (30). The data are plotted in Fig. 6. This essentially represents the shape of the T_1 dispersion curves to be expected in real experiments.

Figure 7 finally shows a comparison between the correlation functions in the strong- and weak-adsorption limits. In the weak-adsorption limit, values $Q_{ads}=0.1\tau^{-1}$ and $Q_{des}=0.9\tau^{-1}$ were assumed for the adsorption and desorption rates, respectively. The exchange correlation function $G_{ex}(t)$ is plotted in the inset. The long-time limit of $G_{ex}(t)$ indicates equilibrium populations deviating by almost two orders of magnitude. The pure orientation correlation functions $G_{reo}(t)$

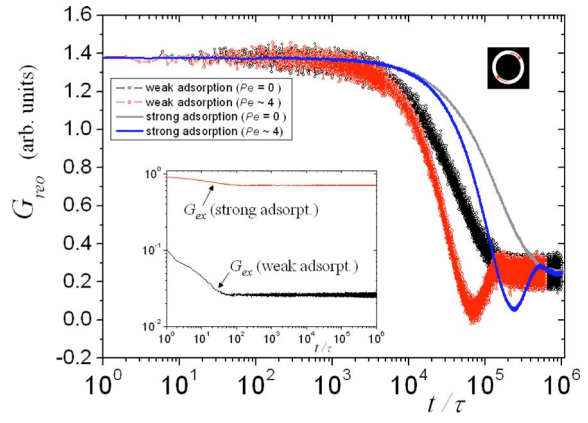

FIG. 7. (Color online) Comparison between the simulated orientation correlation functions in the strong- and weak-adsorption limits in a circular pore. The inset shows the exchange correlation function $G_{ex}(t)$. This function does not vary with flow.

are not that different, but the decay is somewhat faster in the weak-adsorption limit. In the case of weak adsorption the curves are noisy because the relevant particle ensemble is reduced due to the faster exchange with the bulklike phase. That is, there are fewer molecules that are initially and finally in the adsorbed state.

B. Orientational structure factors and simulations for more complex model pore-space structures

The circular channel examined above must be considered as a didactic model revealing the principles of the flow-relaxation effect. Any more realistic pore-space model structure is unavoidably more complex and, as concerns typical porous media, contains random elements. In this sense, two-dimensional random-walk-shaped pipes with smooth [Fig. 2(b)] or rough [Fig. 2(c)] surfaces, and ellipsoidal-grain packs [Fig. 2(d)] will be examined in the subsequent paragraphs as further model pore spaces. In the analytical theory, the topology of the pore space structures can in principle be accounted for by assuming appropriate orientational structure factors [9].

The random character of the pore spaces to be treated may be introduced into the analytical treatment by either a Gaussian distribution about a certain average value k_0 or an equipartition of wave numbers instead of the δ function given in Eq. (26). The orientational structure factor for a Gaussian distribution is given by

$$S(k) = \sqrt{\frac{2}{\pi\epsilon^2}} e^{-(k-k_0)^2/2\epsilon^2}, \tag{35}$$

where ϵ is the standard deviation of $S(k)$. Replacing this function in Eq. (17) leads to the following orientational correlation function:

$$G(t) = \frac{2\pi}{\sqrt{1+2\epsilon^2 D_{disp} t}} e^{-D_{disp} k_0^2 t/(1+2\epsilon^2 D_{disp} t)} \times e^{-(v\epsilon t)^2/2(1+2\epsilon^2 D_{disp} t)} e^{-ik_0 v t/(1+2\epsilon^2 D_{disp} t)}. \tag{36}$$

The velocity v refers to the interface layer where the BMSD process takes place. The dispersion coefficient D_{disp} depends on the flow velocity and the pore geometry. The correlation function Eq. (36) is characterized by three characteristic time constants:

$$\tau_0 = (k_0^2 D_{disp})^{-1}, \tag{37}$$

$$\tau_\epsilon = (2\epsilon^2 D_{disp})^{-1}, \tag{38}$$

$$\tau_v^{Gauss} = (v\epsilon)^{-1}. \tag{39}$$

Another form of the structure factor to be considered here is an equipartition of wave numbers in a certain range [9]:

$$S(k) = \begin{cases} \dfrac{1}{k_u - k_l} & \text{if } k_l \leqslant k \leqslant k_u, \\ 0 & \text{otherwise}, \end{cases} \tag{40}$$

where the upper and lower cutoff values are designated by k_u and k_l, respectively. Inserting this function in Eq. (17) gives

$$G(t) = \frac{\pi^{3/2}}{k_u - k_l} \frac{e^{-v^2 t/4D_{disp}}}{\sqrt{D_{disp} t}} \left(\operatorname{erf}(\sqrt{D_{disp} t} k_u) - \operatorname{erf}(\sqrt{D_{disp} t} k_l) + \frac{e^{-D_{disp} t k_u^2}}{2\pi\sqrt{D_{disp} t} k_u} [1 - \cos(k_u v t)] - \frac{e^{-D_{disp} t k_l^2}}{2\pi\sqrt{D_{disp} t} k_l} [1 - \cos(k_l v t)] \right.$$
$$+ \frac{2}{\pi} e^{-\sqrt{D_{disp} t} k_u} \sum_{n=1}^{\infty} \frac{e^{-(n^2/4)}}{n^2 + 4D_{disp} t k_u^2} f_n^u(x^u, y) - \frac{2}{\pi} e^{-\sqrt{D_{disp} t} k_l} \sum_{n=1}^{\infty} \frac{e^{-(n^2/4)}}{n^2 + 4D_{disp} t k_l^2} f_n^l(x^l, y) + i \frac{e^{-D_{disp} t k_u^2}}{2\pi\sqrt{D_{disp} t} k_u} \sin(k_u v t)$$
$$\left. - i \frac{e^{-D_{disp} t k_l^2}}{2\pi\sqrt{D_{disp} t} k_l} \sin(k_l v t) + i \frac{2}{\pi} e^{-\sqrt{D_{disp} t} k_u} \sum_{n=1}^{\infty} \frac{e^{-(n^2/4)}}{n^2 + 4D_{disp} t k_u^2} g_n^u(x^u, y) - i \frac{2}{\pi} e^{-\sqrt{D_{disp} t} k_l} \sum_{n=1}^{\infty} \frac{e^{-(n^2/4)}}{n^2 + 4D_{disp} t k_l^2} g_n^l(x^l, y) \right), \tag{41}$$

where

$$f_n^{u,l}(x^{u,l}, y) = 2x^{u,l} - 2x^{u,l} \cosh(ny) \cos(2x^{u,l} y) + n \sinh(ny) \cos(2x^{u,l} y), \tag{42}$$

$$g_n^{u,l}(x^{u,l}, y) = 2x^{u,l} \cosh(ny) \sin(2x^{u,l} y) + n \sinh(ny) \cos(2x^{u,l} y). \tag{43}$$

The quantities $x^{u,l}$ and y are defined by $(D_{disp} t)^{1/2} k_{u,l}$ and $\frac{1}{2} v \sqrt{t/D_{disp}}$, respectively. The characteristic time constants are

$$\tau_u = (k_u^2 D_{disp})^{-1}, \tag{44}$$

$$\tau_l = (k_l^2 D_{disp})^{-1}, \tag{45}$$

$$\tau_{\Delta k} = [(\Delta k)^2 D_{disp}]^{-1}, \tag{46}$$

$$\tau_v^{equip} = 4D_{disp}/v^2, \tag{47}$$

where $\Delta k = k_u - k_l$.

1. Random-walk-shaped pipe with smooth surfaces

This pore-space structure consists of two-dimensional straight pipe segments joined in random orientations relative to each other in a nearest-neighbor angle range $-\pi/2 \leqslant \chi$

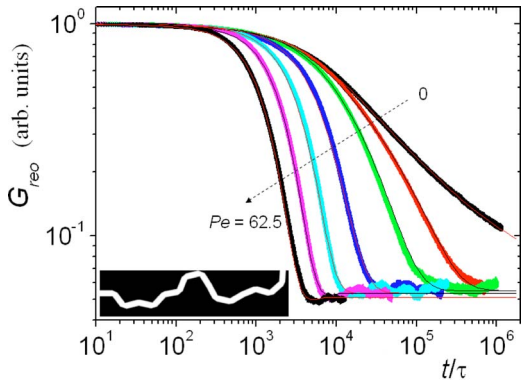

FIG. 8. (Color online) Reorientation autocorrelation function G_{reo} in a random-walk-shaped pipe with smooth surfaces (see lower left corner). The curve parameter is the Péclet number Pe as a measure of the relative flow rate. The values are from the top to the bottom Pe=0.0, 1.25, 2.50, 6.25, 12.5, 25.0, 62.5. The solid lines almost perfectly coinciding with the data points represent fits of Eq. (36) (real part). The resulting parameters are listed in Table II.

$\leqslant \pi/2$ [see Fig. 2(b)]. The segment length $l_{segment}=60\ell$ is short compared to the total system dimensions considered. The pipe width was assumed to be $w=30\ell$. The step width was set as $\sigma=0.2\ell$. The correlation length was evaluated numerically from the segment correlation function $\langle \vec{l}_{segment}(0)\cdot\vec{l}_{segment}(s)\rangle$, where $\vec{l}_{segment}(0)$ and $\vec{l}_{segment}(s)$ are the segment vectors at curvilinear positions 0 and s, respectively. The numerical segment correlation function can be described by an exponential decay plus a constant, that is,

$$\langle \vec{l}_{segment}(0)\cdot\vec{l}_{segment}(s)\rangle \propto \exp\{-s/\xi\} + \text{const.} \qquad (48)$$

The fitted value of the correlation length is $\xi \approx 1.25 l_{segment}$. A random-walk-shaped pipe was also considered by Saffman [28] in a study about hydrodynamic dispersion, and was discussed briefly in Ref. [21].

The time autocorrelation function $G_T(t)$ found with the simulations is characterized by a two-step decay analogous to those shown in Fig. 3. The two steps correspond to the exchange function G_{ex} and the reorientation function G_{reo}. The latter is also plotted in Fig. 8 for different Péclet numbers. These numerically evaluated time correlation functions $G_{reo}(t)$ in Fig. 8 can be well fitted with the real part of Eq. (36), i.e., by assuming a Gaussian structure factor with $\epsilon=0.058\ell^{-1}$ and $k_0=0.053\ell^{-1}$. The fitting parameters are listed in Table II.

The dispersion coefficient increases with the Péclet number as in the case of the circular-pore model. The dependence on the Péclet number can be approximated by (see Fig. 9)

$$D_{disp} \sim \mathrm{Pe}\ln(\mathrm{Pe}). \qquad (49)$$

This result reproduces the behavior reported in Refs. [28,21] where a power law $\sim \mathrm{Pe}^{1.3}$ was stated for a similar range of Péclet numbers in porous media. This sort of behavior is attributed to the so-called boundary-layer dispersion regime [21,29], where diffusion transfers material from the solid walls to faster streamlines.

TABLE II. Values of the parameters in Eq. (36) (real part) fitted to Monte Carlo simulations of the orientation correlation function for the random-walk-shaped pore-space model with smooth surfaces. The wave number and the standard deviation are $k_0=0.053/\ell$ and $\epsilon=0.058/\ell$, respectively.

Péclet number	v (ℓ/τ)	D_{disp} (ℓ^2/τ)
0.00	0.00	1.70×10^{-2}
1.25	6.6×10^{-4}	1.70×10^{-2}
2.50	1.29×10^{-3}	1.70×10^{-2}
6.25	3.19×10^{-3}	1.80×10^{-2}
12.5	5.70×10^{-3}	2.00×10^{-2}
25.0	9.20×10^{-3}	2.50×10^{-2}
62.5	1.49×10^{-2}	4.00×10^{-2}

The characteristic time constants defined in Eqs. (37)–(39) were derived from fits of Eq. (36) to the simulated data and are plotted in Fig. 10(a) as a function of the Péclet number. The parameter τ_v^{Gauss} which accounts for the velocity effect interestingly shows the strongest dependence. The flow velocity, another parameter in Eq. (36), is plotted in Fig. 10(b). As a function of the Péclet number, it grows more slowly than the Péclet number itself and is in all cases smaller than the mean velocity f/w. This finding appears to be plausible since the correlation function always senses the flow behavior in the vicinity of the walls, where the velocity, in the laminar regime, is small. Figure 10(a) also shows the fitted data for τ_v^{equip} defined in Eq. (47) for an equipartition of surface wave numbers. These data were obtained by fitting Eq. (41) to the numerical correlation functions. The velocity effect for an equipartition is obviously much stronger than for a Gaussian distribution of surface wave numbers.

Figure 11 shows the numerical Fourier transforms of the time correlation functions Eq. (35) according to Eq. (18) for the random-walk-shaped pipe model with smooth surfaces. If

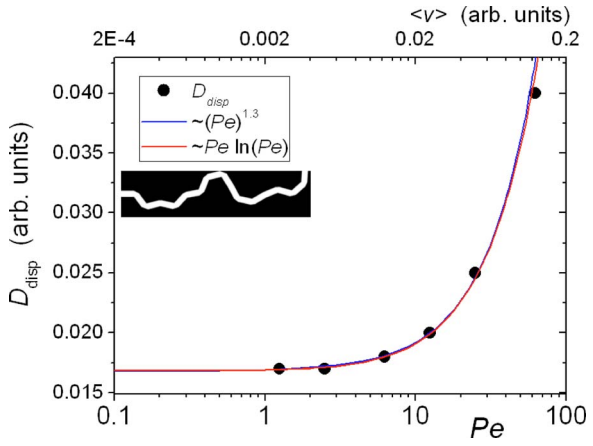

FIG. 9. (Color online) Dispersion coefficient D_{disp} as a function of the Péclet number for the random-walk-shaped pipe model with smooth surface. The data points represent the values obtained by fitting Eq. (36) to the simulated correlation functions. The solid lines represent fits of the laws given in the inset to the data points. Both laws describe the data points very well.

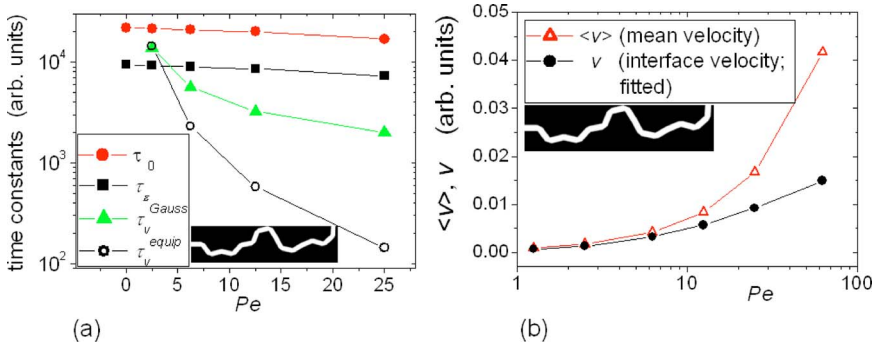

FIG. 10. (Color online) (a) Characteristic time constants defined in Eqs. (37)–(39) as functions of the Péclet number for the random-walk-shaped pipe model with smooth surface (filled data points). The open data points represent data of τ_v^{equip} for an equipartition of wave numbers according to Eq. (47). (b) Flow velocity at the solid liquid interface versus Péclet number for the same pore-space geometry. The data represent fits of Eq. (36) to the simulated correlation functions. All values are smaller than the mean velocity $\langle v\rangle = f/w$. The lines serve to guide the eye.

the pore channel is assumed to have a diameter $w \sim 10^{-6}$ m, and the step time is assumed to be $\tau \sim 10^{-7}$ s, the flow-relaxation effect is expected to become perceptible only below 50 kHz. However, if w is smaller than the above value, the same effect is predicted to occur at higher frequencies.

2. Random-walk-shaped pipe with rough surfaces

This model structure is the same as before but now supplemented with rough surfaces [compare Figs. 2(b) and Fig. 2(c)]. That is, a shorter length scale of the surface topology is introduced whereas the "superstructure" of the random-walk-shaped pipe is maintained. The surface roughness was generated by a sequence of interconnected subsections of length $l_{sub}=0.2\ell \ll l_{segment}$. The angles relative to the superstructure were randomly chosen in the range $-0.9\pi \leqslant \zeta \leqslant 0.9\pi$.

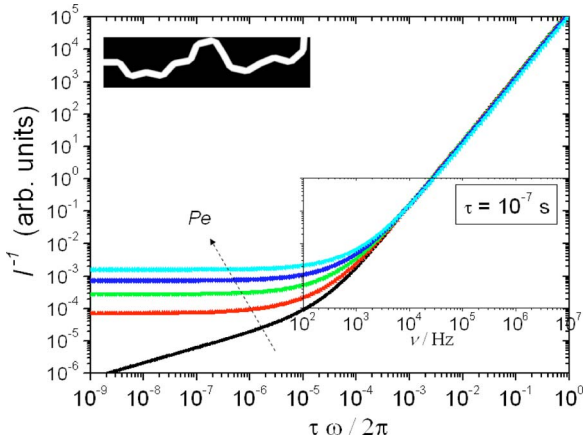

FIG. 11. (Color online) Inverse spectral density versus frequency for different Péclet numbers. The data have been evaluated with Eq. (18) in combination with Eq. (35) for the random-walk-shaped pipe model. The Péclet numbers are from the bottom to the top (see arrow) 0.0,2.5,6.25,12.5,25.0. The coordinate axes of the inset refer to $\tau=10^{-7}$ s so that the frequency axis is now given in hertz. This corresponds to the typical range accessible by the field-cycling NMR relaxometry technique.

The additional effect introduced by the rough border can be identified by simulating the correlation function in a straight channel without random superstructure as shown in Fig. 12. The combined effect of the superstructure and the surface roughness leads to a two-step decay of the orientation correlation function G_{reo} plotted in Fig. 13. The step at short times with little influence of the velocity is due to the surface roughness whereas the superstructure reveals itself as a strongly velocity dependent decay at long times. The surface topology is directly reflected by the bimodal shape of the correlation function decay as visualized in Fig. 13.

The simulated data can be described by a combination of two correlation functions based on Gaussian orientational structure factors for the short- and long-range topologies. Let us term these correlation functions $G_{sr}(t)$ and $G_{lr}(t)$, respectively. Reorientations by the short- and long-range processes occur on very different time scales, so that they can be con-

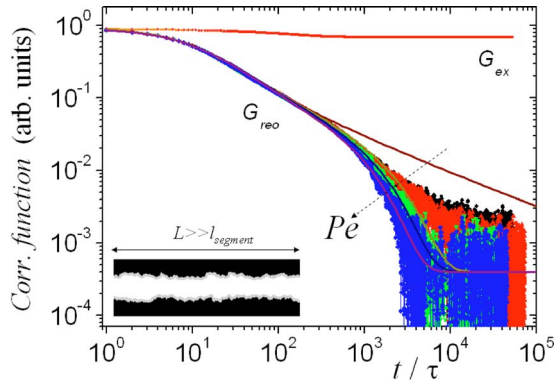

FIG. 12. (Color online) Correlation functions G_{reo} and G_{ex} in a straight pipe with rough borders (see the illustration in the inset). The Monte Carlo simulations were performed for Péclet numbers Pe=0,2.5,12.5,25.0. The exchange correlation function G_{ex} is not perceptibly affected by flow. The relatively weak effect on the orientation correlation function G_{reo} is to be compared with that based on the superstructure with smooth surfaces (see Fig. 8). The combined effect of surface roughness and superstructure will be demonstrated in Fig. 13. The solid lines represent the fits of Eq. (36). With the exception of the static case (Pe=0), the coincidence is almost perfect.

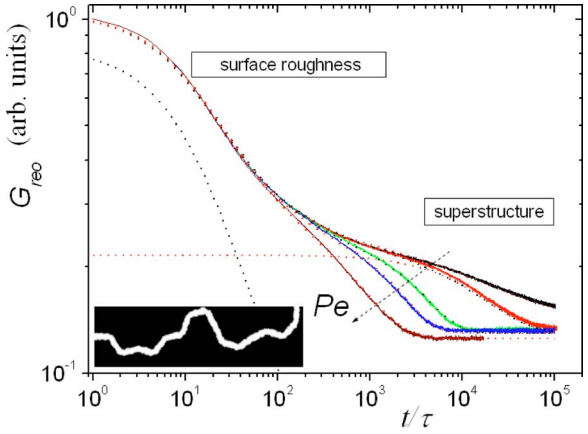

FIG. 13. (Color online) Orientation correlation function G_{reo} in a random-walk-shaped pipe with rough borders (see the illustration in the inset). The Monte Carlo simulations were performed for Péclet numbers Pe=0, 2.5, 12.5, 25.0. The two-step decay reflects the reorientation effects due to the surface roughness at short times and due to the superstructure at long times. The data can be perfectly described by a linear combination of Eqs. (53) and (54). An example is shown by the dotted lines.

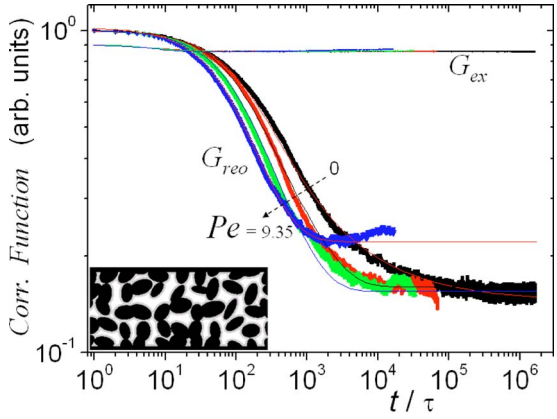

FIG. 14. (Color online) Simulated correlation functions G_{reo} and G_{ex} for the two-dimensional ellipsoidal-grain pack model. The Péclet numbers assumed were Pe=0, 1.92, 4.73, 9.35.

sidered to be stochastically independent. The orientation correlation function can then be expressed by a product according to

$$G_{reo}(t) = \frac{G_T(t)}{G_{ex}(t)} = G_{sr}(t)G_{lr}(t). \tag{50}$$

The short-range term can be analyzed into

$$G_{sr}(t) = g_{sr}(t) + G_{sr}(\infty). \tag{51}$$

The finite quantity $G_{sr}(\infty)$ reflects the anisotropy of the RMTD process on the length scale of surface roughness, whereas $g_{sr}(t)$ represents the proper correlation decay with $g_{sr}(\infty)=0$. On the time scale on which $g_{sr}(t)$ decays to zero, the long-range part remains practically constant under the surface topology conditions considered here, i.e., $G_{lr}(t) \approx G_{lr}(0)$. On this basis, Eq. (50) can be rewritten as

$$\begin{aligned} G_{reo}(t) &= [g_{sr}(t) + G_{sr}(\infty)]G_{lr}(t) \approx g_{sr}(t)G_{lr}(0) + G_{sr}(\infty)G_{lr}(t) \\ &= c_{sr}g_{sr}(t) + c_{lr}G_{lr}(t), \end{aligned} \tag{52}$$

which is approximately a linear combination of the two-time correlation functions with the constant coefficients $c_{sr} \equiv G_{lr}(0)$ and $c_{lr} \equiv G_{sr}(\infty)$.

Let us define a crossover time τ_{co} between the short-range and long-range decay steps of the correlation function so that $g_{sr}(t \gg \tau_{co}) \approx 0$ and $G_{lr}(t \ll \tau_{co}) \approx G_{lr}(0)$. Short-time and long-time limits of the orientation correlation function read then

$$G_{reo}(t) \approx c_{sr}g_{sr}(t) + c_{lr} \quad \text{for } t \ll \tau_{co} \tag{53}$$

and

$$G_{reo}(t) \approx c_{lr}G_{lr}(t) \quad \text{for } t \gg \tau_{co}, \tag{54}$$

respectively. The correlation functions in these two limits may be identified with the correlation functions fitted to the simulation data for a straight pore with rough surfaces (short-time limit) and that fitted to the simulation data for a random-walk-shaped pore (long-time limit). Figure 13 shows a typical example of a superposition of these two functions. The fitting parameters, listed in Table III, show that diffusion at the level of the roughness is not affected by flow.

3. Ellipsoidal-grain packs

As a further model structure a two-dimensional random distribution of ellipsoidal grains in a conducting channel was considered as illustrated in Fig. 2(d). The porosity was evaluated as $p \approx 0.415$ with a mean porous size around 1.1 μm. The correlation length ξ is taken as half the semimajor axis

TABLE III. Values of the parameters in Eq. (36) (real part) fitted to Monte Carlo simulations of the orientation correlation function for the random-walk-shaped pore-space model with rough borders. The wave number and the standard deviation for the superstructure are $k_0=0.053/\ell$ and $\epsilon=0.058/\ell$, respectively. The same parameters corresponding to the short length scale of the structure are $k_0=1.5/\ell$ and $\epsilon=0.84/\ell$, respectively.

Péclet number	v^{long} (ℓ/τ)	D_{disp}^{long} (ℓ^2/τ)	v^{short} (ℓ/τ)	D_{disp}^{short} (ℓ^2/τ)
0.00	0.00	1.00×10^{-2}	0.00	2.60×10^{-2}
2.50	1.10×10^{-3}	1.00×10^{-2}	6.90×10^{-3}	2.60×10^{-2}
12.5	4.50×10^{-3}	1.80×10^{-2}	7.90×10^{-3}	2.40×10^{-2}
25.0	7.70×10^{-3}	2.50×10^{-2}	9.30×10^{-3}	2.40×10^{-2}

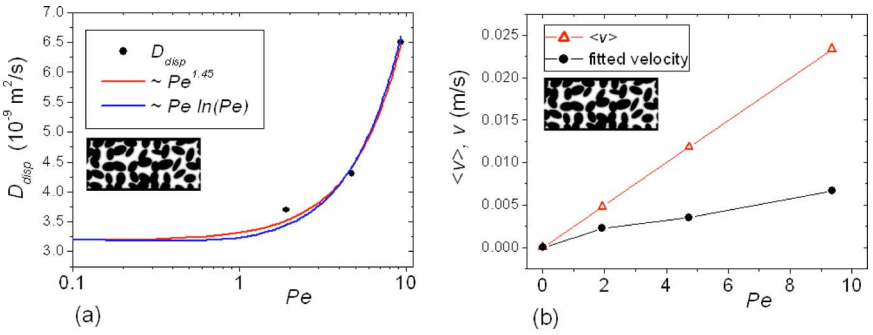

FIG. 15. (Color online) (a) Dispersion coefficients D_{disp} versus Péclet number for the ellipsoidal grain model. The lines have been calculated according to the relationships given in the inset. (b) Flow velocities versus Péclet number in the same model structure. The values fitted to the simulated reorientation autocorrelation functions G_{reo} based on the real part of Eq. (36) tend to be below the mean velocity $\langle v \rangle$.

of the ellipses. The velocity field was imported from the computational fluid dynamics simulation shown in Fig. 2(e). The mean velocity $\langle v \rangle$ is calculated as an average over the magnitudes of this velocity field. The correlation functions can be analyzed into two decay steps by exchange (G_{ex}) and the (flow enhanced) RMTD mechanism (G_{reo}). Figure 14 shows typical examples.

The Gaussian distribution of the orientational structure factor may again be assumed as an analytical representation of the correlation function. The solid lines in Fig. 14 represent fits of the real part of Eq. (36) to the simulated data. The fitting parameters are listed in Table IV.

The dispersion coefficient increases with the Péclet number as shown in Fig. 15(a). In the Péclet number range $0 \leqslant \mathrm{Pe} < 10$ investigated, the effect of molecular Fickian diffusion is comparable to that of convective flow. The data may be described either by a power law $D_{disp} \propto (\mathrm{Pe})^{1.45}$ or by a law $D_{disp} \propto \mathrm{Pe}\ \ln(\mathrm{Pe})$ [see the solid lines in Fig. 15(a)]. The velocity values fitted to the simulated data turned out to be less than the mean velocity as demonstrated in Fig. 15(b).

The inverse spectral density numerically evaluated from Eq. (18) in combination with Eq. (35) is plotted in Fig. 16 as a function of the Péclet number. Assuming the values for the computer unit length and time according to $\ell = 10^{-6}$ m and $\tau = 10^{-7}$ s, respectively, leads to an expected experimental window as shown in the inset box of Fig. 16. According to this, the flow-relaxation effect is expected to show up at frequencies below 100 kHz.

V. DISCUSSION

The effect of hydrodynamic flow on spin-lattice relaxation near solid surfaces was treated analytically and with the aid of Monte Carlo simulations for diverse model situations. Due to the faster surface displacements an enhancement of the spin-lattice relaxation rate is expected in a frequency range where local rotational motions are irrelevant. Experimentally this range can be probed with the aid of the field-cycling NMR relaxometry technique [1]. Judged from the "experimental window" suggested by the inset data shown in Figs. 11 and 16, the effect cannot be expected to be very pronounced. Anyway, a demonstration was possible with water flowing through a Chromolith column as used in high-pressure liquid chromatography [2] although some obvious modifications of the pore surface chemistry encountered in more recent relaxometry experiments with this sort of sample still need to be explained.

The main difficulty one is facing in experimental studies of the flow-relaxation effect is that hydrodynamic flow should be homogeneously distributed in the whole sample in order to achieve the best efficiency. However, hydrodynamic flow tends to occur along certain percolation pathways as demonstrated in the computational fluid dynamics simulation shown in Fig. 2(e). Similar flow patterns were measured in

TABLE IV. Values of the parameters in Eq. (36) (real part) fitted to Monte Carlo simulations of the ellipsoidal-grain pack model. The wave number and the standard deviation are $k_0 = 1.04 \times 10^6$ m^{-1} and $\epsilon = 7.0 \times 10^5$ m^{-1}, respectively.

Péclet number	v (m/s)	D_{disp} (m^2/s)
0.00	0.00	3.1×10^{-9}
1.92	2.228×10^{-3}	3.7×10^{-9}
4.73	3.479×10^{-3}	4.3×10^{-9}
9.35	6.680×10^{-3}	6.5×10^{-9}

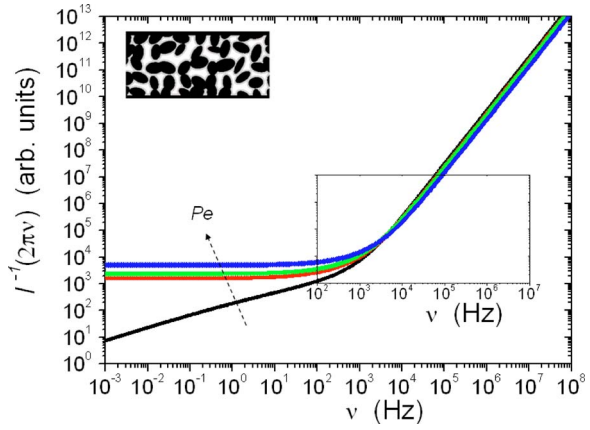

FIG. 16. (Color online) Inverse spectral density versus frequency for different Péclet numbers in the ellipsoidal-grain model. The data represent the numerical Fourier transform of the simulated reorientation autocorrelation function. The frequency scale corresponds to a computer cycle time $\tau \sim 10^{-7}$ s. The Péclet numbers are from the bottom to the top (see arrow) 0,1.92,4.73,9.35. The inset box indicates the typical window accessible in experiments relative to that frequency scale.

percolation model objects with a magnetic resonance microscopy technique [30]. The consequence is that most of the sample volume is not affected by flow of sufficient velocity or is even subject to stagnant zones. What one measures under such conditions is an average relaxation rate between flowing and stagnant material. The flow-relaxation effect is consequently expected little above the experimental error intrinsic to the field-cycling technique.

Mansfield and Issa [31] found in flow mapping experiments in sandstone some stochastic variability of the flow patterns in repeated experiments. This finding may also be relevant for the flow-relaxation effect reported here. It appears that there is some instability of the flow conditions in microscopic pore spaces. Currently we are therefore pursuing a different strategy by employing electroosmotic flow promising more uniform and stable flow velocity distributions.

The flow-relaxation effect can be described theoretically based on the formalism outlined above. For the orientational structure factor an equipartition of wave numbers was assumed [see Eq. (40)]. The distribution of velocities is also approached by an equipartition given by

$$P(v) = \begin{cases} \dfrac{1}{v_{max}} & \text{if } 0 \leqslant v \leqslant v_{max}, \\ 0 & \text{otherwise}, \end{cases} \tag{55}$$

where v_{max} is the upper cutoff value of the velocity distribution. The effective spectral density thus reads

$$I_{equi}(\omega) = \frac{2}{v_{max}(k_u - k_l)} \int_0^{v_{\max}} \int_{k_l}^{k_u} \frac{D_{disp}k^2}{(D_{disp}k^2)^2 + (kv + \omega)^2} dk\, dv. \tag{56}$$

Combining Eqs. (6) and (56) leads to the final expression for the spin-lattice relaxation rate under flow conditions. The lower-cutoff wave number k_l is responsible for the crossover to the low-frequency plateau. The shift of the T_1 data to higher values upon hydrodynamic flow was well reproduced. The upper- and lower-cutoff values of the wave number, k_u and k_l, respectively, indicate the different length scales of the surface orientation. Interestingly these length scales coincide with the bimodal pore size distribution by which Chromolith is specified, that is, "nanometers" corresponding to k_u and "micrometers" corresponding to k_l [2]. The low-frequency spin-lattice relaxation dispersion thus directly reflects features of the surface topology in this way.

VI. CONCLUSIONS

Low-field spin-lattice relaxation of polar liquids filled into a polar, diamagnetic porous medium takes place at the liquid/solid interfaces via the BMSD and RMTD mechanism. This is effectively a surface diffusion process. If hydrodynamic flow is superimposed to molecular diffusion, displacements along surfaces are accelerated in the sense of hydrodynamic dispersion.

There are different aspects that can be associated with this effect. (i) The influence of flow on low-field spin-lattice relaxation can be considered as evidence for the BMSD and RMTD surface relaxation mechanism [3,4]. (ii) Since low-field spin-lattice relaxation in samples of this sort is governed by intramolecular spin interactions [3,4], the relevant fluctuation of the spin interactions is molecular reorientation. That is a sort of rotational analog of Taylor-Aris dispersion [11,12]. (iii) The time scale corresponding to the frequency range on which the flow-relaxation effect occurs implies that the relevant molecular displacements perpendicular to the surface occur on a length scale of a few nanometers only [32]. This may be regarded as an example of "nanofluidics near surfaces" [33]. (iv) There is a discussion in the literature about the relevant interfacial boundary condition [34]. Judged from the present results, one is dealing with a modified interfacial slip boundary condition in the sense that molecules move in a sort of hopping process along the surfaces (see the illustration in Fig. 1).

These findings can be considered to be relevant for high-pressure liquid chromatography and catalysis applications where surface transport and molecular exchange play a crucial role [35,36]. The adsorption-desorption cycles on surfaces underlying the flow-relaxation effect are also of some theoretical interest, since anomalous or superdiffusive Lévy-walk-like behavior was predicted for such scenarios [5,37]. The flow-relaxation effect may open a wide field of potential studies of nanometric surface effects provided that samples and experimental setups permitting stable and uniform flow patterns along curved surface topologies are established.

ACKNOWLEDGMENTS

Bogdan Buhai has contributed the computational fluid dynamics simulation. The authors thank Esteban Anoardo and Hans Wiringer for discussions and assistance. This work was funded by the Deutsche Forschungsgemeinschaft.

[1] R. Kimmich and E. Anoardo, Prog. Nucl. Magn. Reson. Spectrosc. **44**, 257 (2004).
[2] C. Mattea and R. Kimmich, Phys. Rev. Lett. **94**, 024502 (2005).
[3] S. Stapf, R. Kimmich, and R.-O. Seitter, Phys. Rev. Lett. **75**, 2855 (1995).
[4] T. Zavada and R. Kimmich, J. Chem. Phys. **109**, 6929 (1998).
[5] O. V. Bychuk and B. O'Shaughnessy, J. Chem. Phys. **101**, 772 (1994).
[6] R. Valiullin, R. Kimmich, and N. Fatkullin, Phys. Rev. E **56**, 4371 (1997).
[7] P. Levitz, E. Lecolier, A. Mourchid, A. Delville, and S. Lyonnard, Europhys. Lett. **49**, 672 (2000).
[8] J. A. Revelli, C. E. Budde, D. Prato, and H. S. Wio, New J. Phys. **7**, 15 (2005).
[9] R. Kimmich and H. W. Weber, Phys. Rev. B **47**, 11788 (1993).

[10] M. Vilfan and M. Vuk, J. Chem. Phys. **120**, 8638 (2004).
[11] G. I. Taylor, Proc. R. Soc. London, Ser. A **219**, 186 (1953).
[12] R. Aris, Proc. R. Soc. London, Ser. A **235**, 67 (1956).
[13] A. Compte and J. Camacho, Phys. Rev. E **56**, 5445 (1997).
[14] M. G. Gauthier, G. W. Slater, and K. D. Dorfman, Eur. Phys. J. E **15**, 71 (2004).
[15] M. Al-Ghoul and B. C. Eu, Phys. Rev. E **70**, 016301 (2004).
[16] D. Kandhai, D. Hlushkou, A. G. Hoekstra, P. M. A. Sloot, H. Van As, and U. Tallarek, Phys. Rev. Lett. **88**, 234501 (2002).
[17] H. Schwarze, U. Jaekel, and H. Vereecken, Transp. Porous Media **43**, 265 (2001).
[18] C. P. Lowe and D. Frenkel, Phys. Rev. Lett. **77**, 4552 (1996).
[19] A. Abragam, *The Principles of Nuclear Magnetism* (Clarendon Press, Oxford, 1961).
[20] R. Kimmich, *NMR Tomography, Diffusometry, Relaxometry* (Springer, Berlin, 1997).
[21] M. Sahimi, *Flow and Transport in Porous Media and Fractured Rock* (VCH, Weinheim, 1995); Rev. Mod. Phys. **65**, 1393 (1993).
[22] F. A. L. Dullien, *Porous Media: Fluid Transport and Pore Structure* (Academic Press, San Diego, 1992).
[23] L. de Arcangelis, J. Koplik, S. Redner, and D. Wilkinson, Phys. Rev. Lett. **57**, 996 (1986).
[24] J. C. Bacri, N. Rakotomalala, and D. Salin, Phys. Rev. Lett. **58**, 2035 (1987).
[25] J. Klafter, M. F. Shlesinger, and G. Zumofen, Phys. Today **49**(2), 33 (1996).
[26] E. Anoardo, F. Grinberg, M. Vilfan, and R. Kimmich, Chem. Phys. **297**, 99 (2004).
[27] R.-O. Seitter, T. Link (Zavada), R. Kimmich, A. Kobelkov, P. Wolfangel, and K. Müller, J. Chem. Phys. **112**, 8715 (2000).
[28] P. G. Saffman, J. Fluid Mech. **6**, 321 (1959).
[29] D. L. Koch and J. F. Brady, J. Fluid Mech. **154**, 399 (1985).
[30] A. Klemm, R. Kimmich, and M. Weber, Phys. Rev. E **63**, 041514 (2001).
[31] P. Mansfield and B. Issa, J. Magn. Reson., Ser. A **122**, 137 (1996).
[32] Y. Leng, P. T. Cummings, Phys. Rev. Lett. **94**, 026101 (2005).
[33] K. P. Travis and K. E. Gubbins, J. Chem. Phys. **112**, 1984 (2000).
[34] L. Léger, J. Phys.: Condens. Matter **15**, S19 (2003).
[35] M. Krucker, A. Lienau, K. Putzbach, M. D. Grynbaum, P. Schuler, and K. Albert, Anal. Chem. **76**, 2623 (2004).
[36] M. Coppey, O. Bénichou, J. Klafter, M. Moreau, and G. Oshanin, Phys. Rev. E **69**, 036115 (2004).
[37] A. M. Lacasta, J. M. Sancho, A. H. Romero, I. M. Sokolov, and K. Lindenberg, Phys. Rev. E **70**, 051104 (2004).